The Astrophysical Journal, 654:665–674, 2007 January 1
© 2007. The American Astronomical Society. All rights reserved. Printed in U.S.A.

ENERGY RELEASE RATES ALONG Hα FLARE RIBBONS AND THE LOCATION OF HARD X-RAY SOURCES

M. Temmer
Hvar Observatory, Zagreb, Croatia

A. M. Veronig
IGAM–Institute of Physics, University of Graz, Austria

B. Vršnak
Hvar Observatory, Zagreb, Croatia

and

C. Miklenic
IGAM–Institute of Physics, University of Graz, Austria
Received 2006 August 2; accepted 2006 September 19

ABSTRACT

Local reconnection and energy release rates for an X3.8 flare that occurred on 2005 January 17 are derived. In particular, we distinguish between Hα flare ribbon segments that were accompanied by *RHESSI* hard X-ray (HXR) footpoints and those without HXRs. We find that the reconnection and energy release rates are not uniform along the flare ribbons but much larger at the locations where the HXR footpoints are observed. The difference is about 2 orders of magnitude in the case of the energy release rates and 1 order of magnitude for the reconnection rates (with peak values up to 8 kV m^{-1}). These differences are enough to explain the different flare morphologies typically observed in HXRs (compact footpoints) and Hα/UV (extended ribbons) by the limited dynamic range of present HXR instruments. Our results are consistent with a scenario in which the electrons are accelerated primarily along a certain subsystem of magnetic loops as outlined by the HXR footpoints, and only a minor fraction (for the 2005 January 17 flare estimated to be about 1/15) go into the large flare arcade outlined by the Hα ribbons and EUV postflare loops.

Subject headings: Sun: flares — Sun: magnetic fields — Sun: X-rays, gamma rays

Online material: color figure, mpeg animation

1. INTRODUCTION

In the classical picture of the flare energy release, referred to as the "CSHKP" model (Carmichael 1964; Sturrock 1966; Hirayama 1974; Kopp & Pneuman 1976), an erupting filament distorts the overlying coronal magnetic field lines, which are stretched to form a vertical current sheet. In this current sheet, coronal magnetic field lines successively reconnect, which results in a growing flare/postflare loop system and separating Hα and UV flare ribbons, as observed in many flares (e.g., Švestka et al. 1987; Tsuneta et al. 1992; Švestka 1996; Fletcher & Hudson 2001; Krucker et al. 2003; Asai et al. 2004; Sui et al. 2004; Veronig et al. 2006a; Vršnak et al. 2006). The model depicts the reconfiguration of the coronal magnetic fields and the associated conversion of free magnetic energy into kinetic energy, heating, and particle acceleration.

Forbes & Priest (1984) and Forbes & Lin (2000) pointed out that in such a two-dimensional model (with translational symmetry in the third dimension), the local reconnection rate, i.e., the rate at which magnetic field lines are swept into the reconnection region where they break and reconnect, is given by the coronal electric field E_c at the reconnection site, and can be inferred from the observed flare ribbon separation speed $v_{\rm fl}$ and the local longitudinal photospheric magnetic field B_p:

$$E_c = v_{\rm fl} B_p. \tag{1}$$

The released magnetic energy rate dW/dt comes from the Poynting flux S into the reconnection region, $dW/dt = A_r S$, where A_r denotes the area of the current sheet (Isobe et al. 2002). Taking into account magnetic flux conservation ($v_{\rm in} B_c = v_{\rm fl} B_p$, where $v_{\rm in}$ is the plasma inflow velocity into the reconnection region) and assuming that the coronal magnetic field B_c maps linearly to the photospheric magnetic field B_p, $B_c = aB_p$, with the proportionality factor $a < 1$ assumed constant in the flaring region, the Poynting flux into the reconnection region can be estimated from the observations as (Isobe et al. 2002; Asai et al. 2004)

$$|\boldsymbol{S}| = \left|\frac{2}{\mu}(\boldsymbol{E}_c \times \boldsymbol{B}_c)\right| = \frac{2}{\mu} v_{\rm fl} B_p B_c = \frac{2a}{\mu} v_{\rm fl} B_p^2. \tag{2}$$

Assuming further that A_r does not significantly change during the impulsive phase of the flare, the energy release rate is proportional to the Poynting flux: $dW/dt \propto S \propto v_{\rm fl} B_p^2$ (for further discussions see, e.g., Asai et al. 2004; Miklenic et al. 2006; Lee et al. 2006).[1] These are obviously simplifying assumptions, but they should be reasonable, in particular considering that we are not interested in the absolute values of E_c and dW/dt but in their relative contributions from different parts along the flare ribbons.

The enormous amount of energy released during the magnetic reconnection process in solar flares (up to 10^{25} J) goes into acceleration of particles to suprathermal velocities, plasma heating,

[1] Note that in the paper by Lee et al. (2006) a slightly different expression was derived for dW/dt by linking the time dependent area of the reconnecting current sheet, A_r, to the observed flare kernel area, $A_{\rm fl}$, while assuming the aspect ratio of the current sheet constant: $dW/dt \propto v_{\rm fl} B_p^2 A_{\rm fl}$.

and mass motions. It is generally accepted that hard X-ray (HXR) sources map to the primary energy release site in solar flares, where particle acceleration is assumed to occur (e.g., Fletcher & Hudson 2001), and thus give insight into the energy release process. The flare HXR emission is mainly concentrated at the footpoints of magnetic loops (e.g., Hoyng et al. 1981; Sakao 1994), and is assumed to be produced by accelerated electrons that are collisionally stopped in the "dense" chromosphere (as compared to the tenuous corona) and emit nonthermal thick-target bremsstrahlung when braking in the field of the ions (Brown 1971).[2]

Comparison of HXR sources with Hα and UV images shows that most often the HXR emission is concentrated in two or more compact sources, which cover only a small part of the flare ribbon, predominantly associated with bright Hα (UV) kernels located on the outer edge of the ribbons (e.g., Hoyng et al. 1981; Sakao et al. 1992; Asai et al. 2004; Kašparová et al. 2005; Krucker et al. 2005). Only rare exceptions seem to show "HXR ribbons" (for an example see Masuda et al. 2001). There are basically two different scenarios accounting for the different source morphologies observed in chromospheric HXRs as compared to Hα and UV. (1) In contrast to the chromospheric HXR emission that is solely due to precipitating electrons, Hα and UV flare emission can be excited by electron bombardment but also by other processes, such as heat flux from the hot flaring corona (see, e.g., Kitahara & Kurokawa 1990; Czaykowska et al. 1999; Fletcher & Hudson 2001). (2) The limited dynamic range of X-ray instruments may lead to the effect that only the strongest nonthermal sources are observed in HXRs, whereas the weaker ones are buried in the noise of the instruments. Scenario 1 implies that the electrons are accelerated solely along a small subset of loops, whereas other energy transport mechanisms such as thermal conduction fronts occur along the whole arcade outlined by the chromospheric Hα (UV) flare ribbons and the coronal soft X-ray and EUV (post)flare arcade system; i.e., the flare ribbon segments accompanied by HXRs are produced by a different mechanism than those not accompanied by HXR sources. In this picture, the released energy may be equally partitioned into particle acceleration and direct plasma heating. Scenario 2 implies that the whole flare ribbon is heated by accelerated electrons. The electrons are accelerated along the whole arcade system but a substantial fraction of the beam is focused along the loop subsystem mapped by the compact HXR sources. In this case, the energy released by magnetic reconnection goes predominantly into acceleration of suprathermal particles.

In this paper, we study the X3.8 flare of 2005 January 17 (centered at N14°, W25°) that was observed in X-rays by the *Ramaty High-Energy Solar Spectroscopic Imager* (*RHESSI*; Lin et al. 2002) and in Hα by the Hvar and Kanzelhöhe Observatories. The flare reveals a complex morphology in X-rays with up to four distinct HXR footpoint sources observed simultaneously. Our main aim is to investigate what distinguishes those parts of the Hα ribbons that coincide with HXR sources from those not accompanied by HXR footpoints. This aim will be accomplished by deriving local reconnection rates and energy release rates at ribbon locations associated with HXR sources and comparing them with those derived at ribbon locations that are not accompanied by HXRs. This investigation is along the line of a case study carried out by Asai et al. (2002, 2004) using *Yohkoh* HXR images combined with Hα observations in order to infer energy release rates at different ribbon locations for an X-class flare showing a "simple" two-footpoint morphology in HXRs. These authors found that the derived energy release rates were about a factor of 20 higher associated with Hα kernels that are accompanied by HXR sources than for those without. They concluded that this difference is enough to explain the different source appearances in Hα and HXRs by the *Yohkoh* dynamic range (i.e., their outcome supports scenario 2).

[2] However, for some events observed by *Yohkoh* and *RHESSI* there is evidence for nonthermal hard X-rays from the corona (Masuda et al. 1994; Lin et al. 2003; Veronig & Brown 2004).

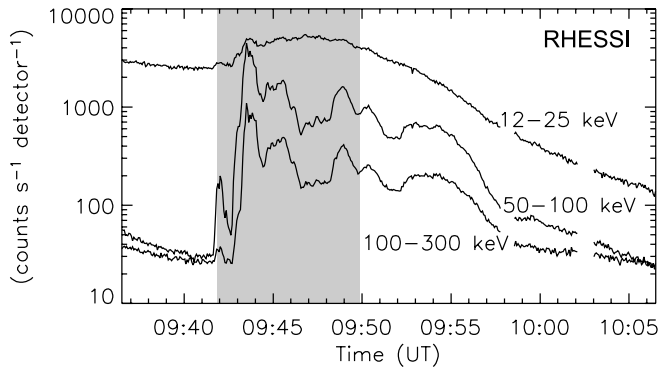

FIG. 1.—*RHESSI* count rates in three energy bands (12–25, 50–100, and 100–300 keV). The period covered by HO high-cadence Hα imaging is indicated by the shaded bar. [*See the electronic edition of the Journal for a color version of this figure.*]

The paper is structured as follows. In § 2 we describe the data set and the applied methods. In § 3.1 the source morphology and evolution of the flare as observed in Hα and *RHESSI* HXRs is studied. In § 3.2 we present the local reconnection rates and energy release rates derived from the Hα ribbon expansion velocity v_{fl} and the local photospheric magnetic field B_p along four different tracking paths (P1–P4) in each magnetic polarity domain. P1 and P2 are chosen to intersect with the strongest HXR footpoint source in each magnetic polarity, P3 lies on the periphery of this HXR sources, and P4 lies basically outside of any HXR footpoint source. The obtained results are discussed in § 4.

2. DATA AND METHODS

We study the X3.8/3B flare of 2005 January 17 with emphasis on the major peak that occurred between ~9:40 and 10:05 UT. The entire evolution of this LDE flare is quite complex and includes several stages of enhanced emission. The *GOES* soft X-ray flux shows a sudden increase to M2 level around 8:00 UT, then gradually increases to the X2 level, and finally (starting around ~09:43 UT) shows an impulsive enhancement that reaches the X3.8 peak at 09:52 UT. For a more detailed description of this event and the associated Moreton/EIT wave, we refer to Veronig et al. (2006b).

During the major peak of this LDE flare, X-ray data from *RHESSI* (Lin et al. 2002) reveal a series of strong HXR bursts (see Fig. 1). In order to minimize pulse pileup effects in this intense event, the *RHESSI* thick attenuators were brought into in the field of view, causing a rapid drop of the effective detector area at low photon energies (Smith et al. 2002). For the analysis, we use series of *RHESSI* images reconstructed with the CLEAN algorithm in the 30–100 keV energy band with 20 s (~5 *RHESSI* rotations) integration excluding intervals of shutter movements (Hurford et al. 2002). Several cubes were reconstructed during the time interval 09:41:40–10:04:40 UT using front detector segments 3–8 and 2–8, and using the uniform and natural weighting schemes, respectively. The flare shows a complex HXR morphology with

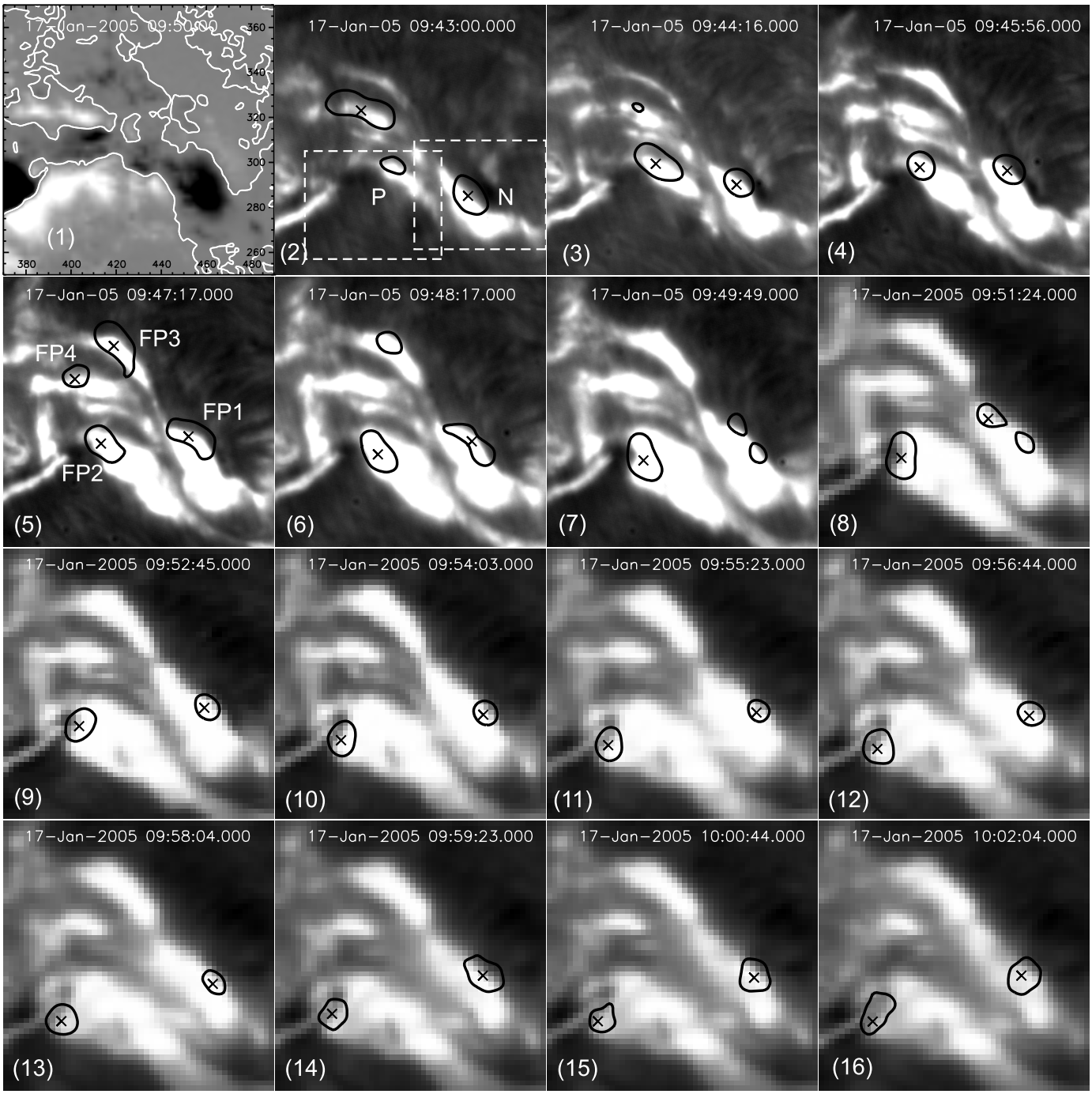

FIG. 2.—Evolution of the Hα flare ribbons (*panels 2–16*) and the longitudinal photospheric magnetic field measured by MDI (*panel 1*). The white lines in panel 1 indicate the magnetic inversion lines. Panels 2–7 show Hα filtergrams from HO; panels 8–16 show Hα − 0.3 Å filtergrams from KSO. On each Hα image, the 40% contours of the closest-in-time *RHESSI* 30–100 keV HXR image together with the source centroids (*crosses*) are overlaid. The two boxes (P, N) drawn in panel 2 outline the field of view shown in the two panels of Fig. 4.

up to four sources simultaneously present, but two main sources prevail during the overall flare impulsive phase (see Fig. 2).

High time cadence Hα imagery is available from the Kanzelhöhe Solar Observatory (KSO),[3] Austria, as well as from the Hvar Observatory (HO), Croatia. KSO routinely takes full-disk Hα images with a time cadence of ∼5 s and a spatial resolution of 2.2″ pixel^{-1}. When the flare mode is triggered, also off-band filtergrams at Hα − 0.3 Å and Hα + 0.4 Å are taken with a cadence of about 1 image per minute (Otruba & Pötzi 2003). The HO performs campaign observations of active regions with a field of view of about 300″ × 300″ with a pixel resolution of 0.3″ pixel^{-1} and a time cadence of ∼4 s (Otruba 2005). For the Hα flare ribbon separation measurements, image series with high spatial resolution and high time cadence are preferred. Therefore, we use the HO data although they cover only the impulsive flare phase from 09:41:50 to 09:49:50 UT (indicated in Fig. 1). The KSO images acquired in the Hα line core are strongly saturated during the impulsive flare phase, whereas the KSO Hα off-band images

[3] See http://cesar.kso.ac.at.

(less saturated) have a too low time cadence (~60–80 s) for the present type of analysis. However, we use the KSO Hα − 0.3 Å and Hα + 0.4 Å off-band filtergrams for context observations.

Figure 2 shows the evolution of the whole impulsive flare phase as observed in HO Hα, KSO Hα − 0.3 Å, and *RHESSI* 30–100 keV HXRs. The *RHESSI* contours are from the images reconstructed with front detectors 2–8 using the natural weighting scheme. On each Hα image, the 40% contour of the maximum intensity of the nearest-in-time *RHESSI* image is overlaid together with the derived source centroids. The source centroids were calculated as the center of gravity along the *xy*-intensity distribution within 60% of the maximum intensity of each image. Note that for the calculation of the source centroids, we used *RHESSI* images reconstructed with front detectors 3–8, giving a lower angular resolution than those reconstructed with detectors 2–8. In general, the source centroids derived using images reconstructed with detectors 2–8 are similar to those of detectors 3–8 (as can be inferred from Fig. 2), but the centroids derived with detectors 3–8 yielded more stable results in cases of low count statistics.

Photospheric magnetic field measurements are taken from the Michelson Doppler Imager (MDI; Scherrer et al. 1995) instrument aboard the *Solar and Heliospheric Observatory* (*SOHO*). For the study, we used the nearest-in-time full-disk longitudinal magnetogram acquired at 09:39:02 UT with a spatial resolution of $\sim 2''$ pixel^{-1}. As recently pointed out by Berger & Lites (2003) MDI can drastically underestimate the magnetic field strength. To take into account this underestimation, the original MDI data values were divided by the mean correction factor of 0.69 reported in Berger & Lites (2003). To measure for each selected pixel on the Hα ribbon the corresponding magnetic field, the MDI image was coregistered to the HO images; i.e., the MDI pixels have been interpolated to the finer HO Hα pixel scale. For context information as well as for alignment purposes, also a white-light (WL) image from the *Transition Region and Coronal Explorer* (*TRACE*; Handy et al. 1999) at 10:09:43 UT was used.

The different image data sets were co-aligned by two different methods: (1) calculating cross-correlation coefficients from image subfields (see Fletcher & Hudson 2001), and (2) manually co-aligning distinct structures within each image. Before the alignment, all image data sets were differentially rotated to the same reference time, oriented to solar north up, and interpolated to the same pixel scale. As the easiest part, both Hα data sets (HO and KSO) were aligned. The alignment of the MDI magnetogram with the Hα filtergrams was done through KSO Hα off-band images (revealing also photospheric structures) and an MDI continuum image. The same MDI continuum image was also used for the alignment with the *TRACE* WL image. The *RHESSI* images were aligned by matching distinct HXR sources to localized Hα brightenings as observed in the KSO Hα off-band images. From this procedure, we can finally calculate the offsets between *RHESSI* and MDI/*TRACE*. As a cross-check, we used a *TRACE* 1600 Å flare image and co-aligned it with *RHESSI* and KSO Hα off-band images by matching distinct brightenings. The calculations using this latter method led to the same offsets as achieved from the former method within an accuracy of $\sim 2''$.

To measure the flare ribbon separation velocity v_{fl}, we tracked the apparent motion of the outer edge of the two main Hα flare ribbons along four different tracking paths (P1–P4). The studied tracking paths are indicated in Figure 4 for the ribbon in the negative (*top panel*) and positive (*bottom panel*) magnetic polarity, respectively. The paths are distinguished in that some of them are accompanied by HXR sources whereas others are not (or only weakly): P1 and P2 were chosen to directly cross the centroids of the main HXR footpoints, the P3 paths lie on the periphery of the HXR footpoints, and the P4 paths are basically located outside any HXR source. To follow the evolution of the Hα ribbons, 85% contour levels with respect to the maximum intensity in each image were used in order to define the outer edge of the ribbon fronts. Then the intersection points between the ribbon fronts and the defined tracking path along the direction of ribbon expansion were measured. Combined with the magnetic field B_p at that location, this allows us to estimate the associated local reconnection rate $E_c = v_{\mathrm{fl}} B_p$ and energy release rate $dW/dt \propto S \propto v_{\mathrm{fl}} B_p^2$ at each instant.

3. RESULTS

3.1. *Source Morphology and Motions*

Figure 2 shows the morphology and evolution of the flare sources observed in Hα and HXRs. Up to four individual HXR footpoints (indicated as FP1–FP4 in panel 5) are present simultaneously along the four most intense Hα ribbon segments, arranged in a quadrupolar manner. FP1 and FP3 are situated in negative, FP2 and FP4 in positive magnetic polarity fields. However, only two HXR footpoints (FP1 and FP2) prevail during the overall flare impulsive phase. The HXR sources are predominantly located on the outer edges of the expanding Hα ribbons. This is consistent with the CSHKP model, in that the outermost edges of the flare ribbons map to the newly reconnected field lines along which the released energy is channeled, whereas the inner parts that map to earlier reconnected field lines are already cooling. However, the situation seems to be more complex for the ribbon associated with FP2. In Hα, a tongue-like feature develops, and the HXR footpoint FP2 apparently moves along with it.

While the expansion of the Hα ribbons is mainly perpendicular to the magnetic inversion line, the two dominant HXR footpoints (FP1 and FP2) show in addition to this outward motion also a component parallel to the neutral line (see Fig. 2). As revealed from several *Yohkoh* HXT and *RHESSI* studies, such HXR source motions parallel to the inversion line (whereby the footpoints can separate or converge) seem to be quite common (e.g., Sakao et al. 1998; Fletcher & Hudson 2002; Krucker et al. 2003; Grigis & Benz 2005; Bogachev et al. 2005). These parallel motions cannot be explained within the standard 2D picture of magnetic reconnection. They may be due to a highly sheared magnetic field configuration or they may reflect that at each instant the electrons are being preferentially accelerated along certain loop subsystems, whereas the Hα ribbons outline the whole arcade field involved in the reconnection process.

For clearer demonstration of the HXR source motions in the 2005 January 17 flare and their relation to the active region and underlying magnetic field, we show in Figure 3 the *RHESSI* HXR source centroids overlaid on a *TRACE* WL image (*top panel*) and on an MDI magnetogram (*bottom panel*). As it can be seen in the MDI image, the HXR sources tend to move along iso-Gaussian lines. The WL image shows that the two main footpoints are located at the inner parts of the sunspots penumbrae. Partly they even intrude into the umbra (FP1), but seem to avoid the umbra's innermost part, i.e., the regions of strongest fields. The penumbral magnetic field strengths associated with the HXR source centroids lie in the range of about [+600, +1500] and [−600, −1600] G. Source centroids of FP1 that are close to or slightly within the umbra are associated with magnetic fields of about −2000 G.

3.2. *Local Reconnection and Energy Release Rates*

Figure 4 shows Hα images of the flare ribbons associated with the main HXR sources FP1 (*top panel*) and FP2 (*bottom panel*), respectively, together with the *RHESSI* source centroids and the

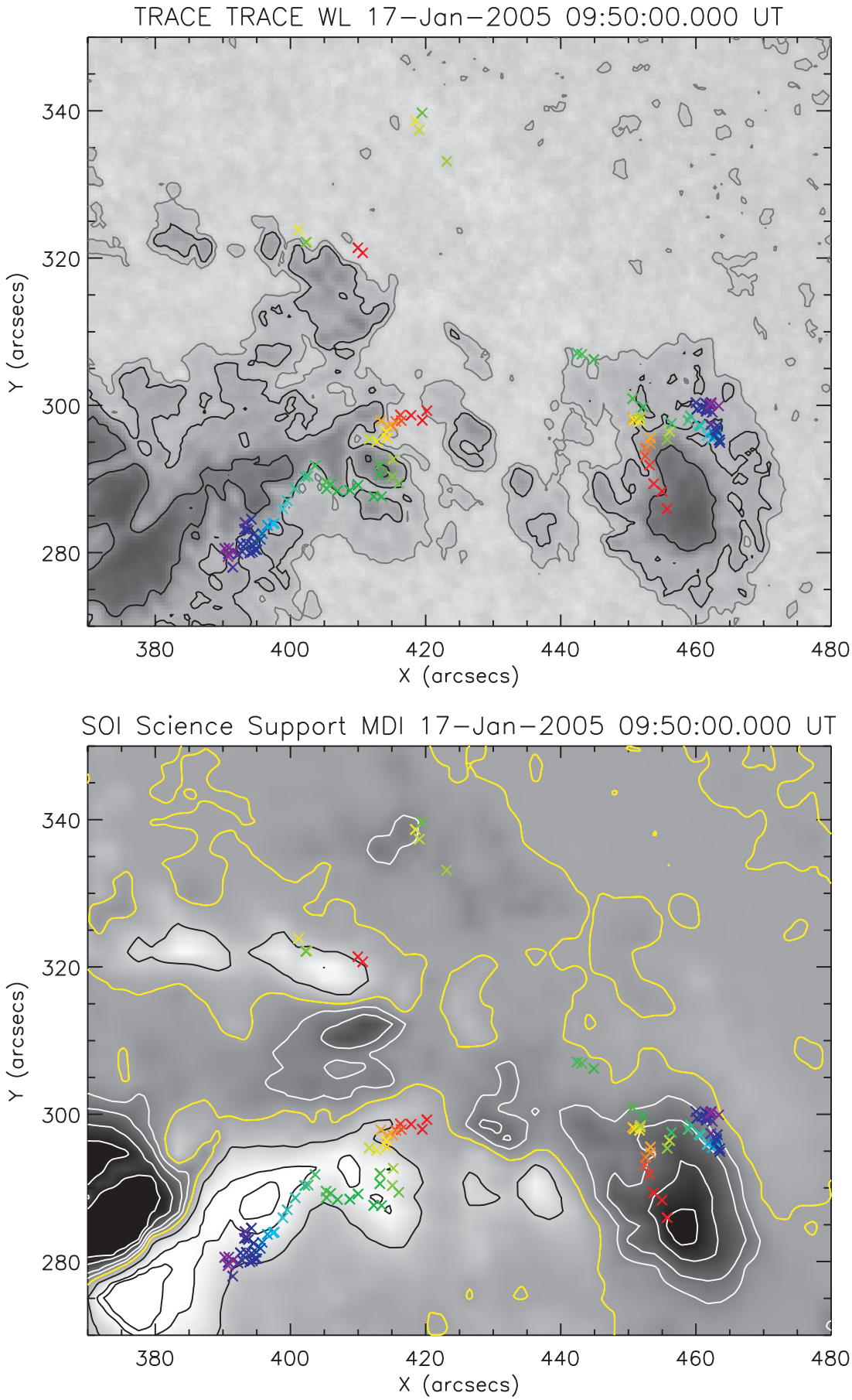

FIG. 3.—HXR source centroids overlaid on a *TRACE* WL image (*top*) and MDI magnetogram (*bottom*). The subsequent occurrence of the HXR sources from 09:43:20 to 10:04:10 UT is color coded from red to purple. *Top*: *TRACE* WL contours roughly outline the umbrae as well as inner and outer penumbrae of the sunspots. *Bottom*: Iso-Gaussian lines of −2000, −1600, −1300, and −600 G (*white contours*) and +600, +1300, and +1500 G (*black contours*) are indicated. The yellow line marks the magnetic inversion line. [*This figure is available as an mpeg animation in the electronic edition of the Journal.*]

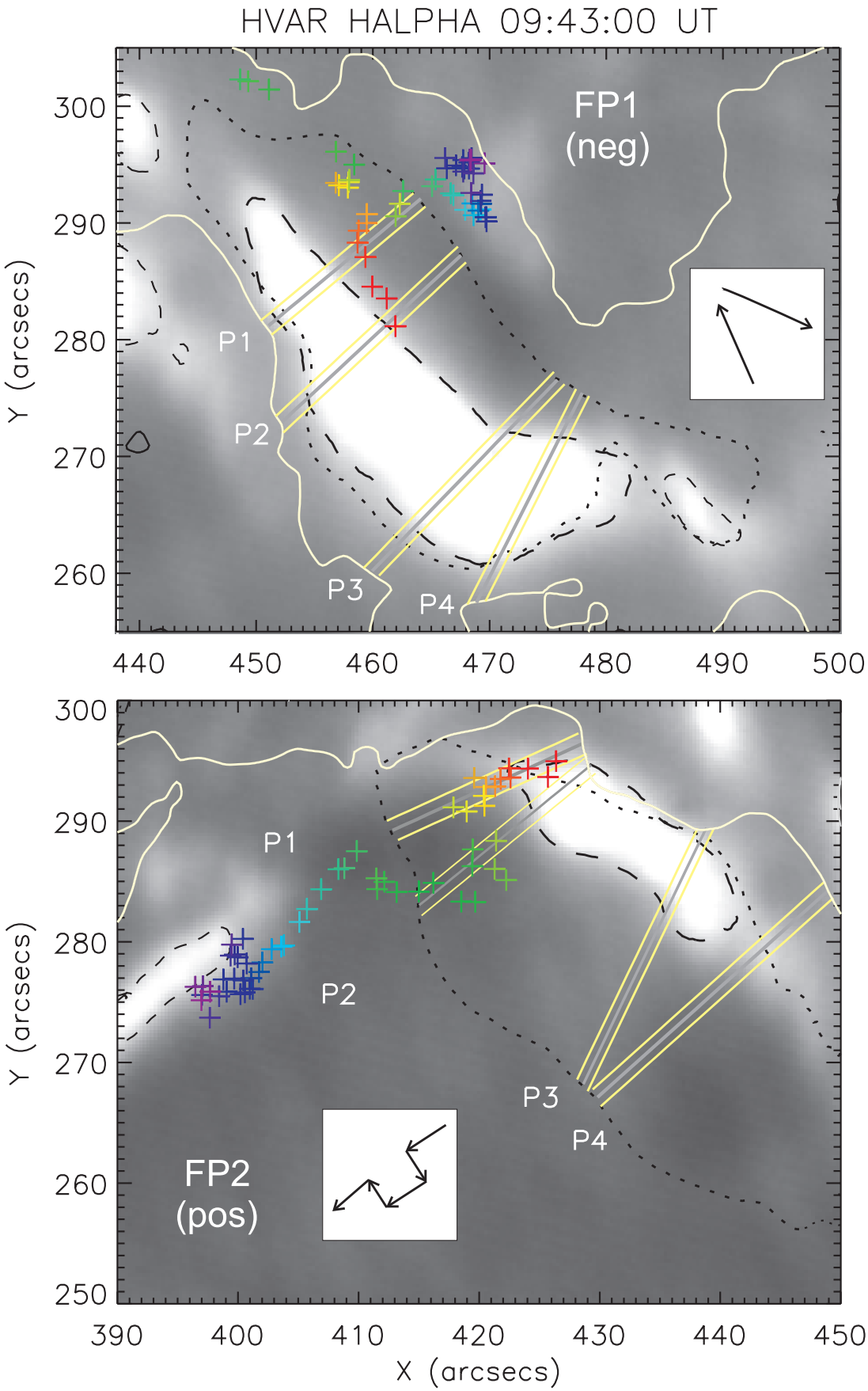

FIG. 4.—For each flare ribbon associated with the major HXR sources (FP1 and FP2), we show the four different tracking paths (P1–P4) along which the ribbon expansion was followed. The top panel shows the ribbon associated with FP1 (situated in negative polarity); the bottom panel shows the ribbon associated with FP2 (situated in positive polarity). The underlying images show subfields of the HO Hα image acquired at 09:43:00 UT (the plotted subfields are indicated in panel 2 of Fig. 2). The crosses show the evolution of the HXR centroids color coded in time from red to purple; white lines indicate the magnetic inversion lines, the dotted line indicates the contour of the last Hα ribbon used in the analysis, and in the inserts the main directions of motion of the HXR sources are schematically drawn.

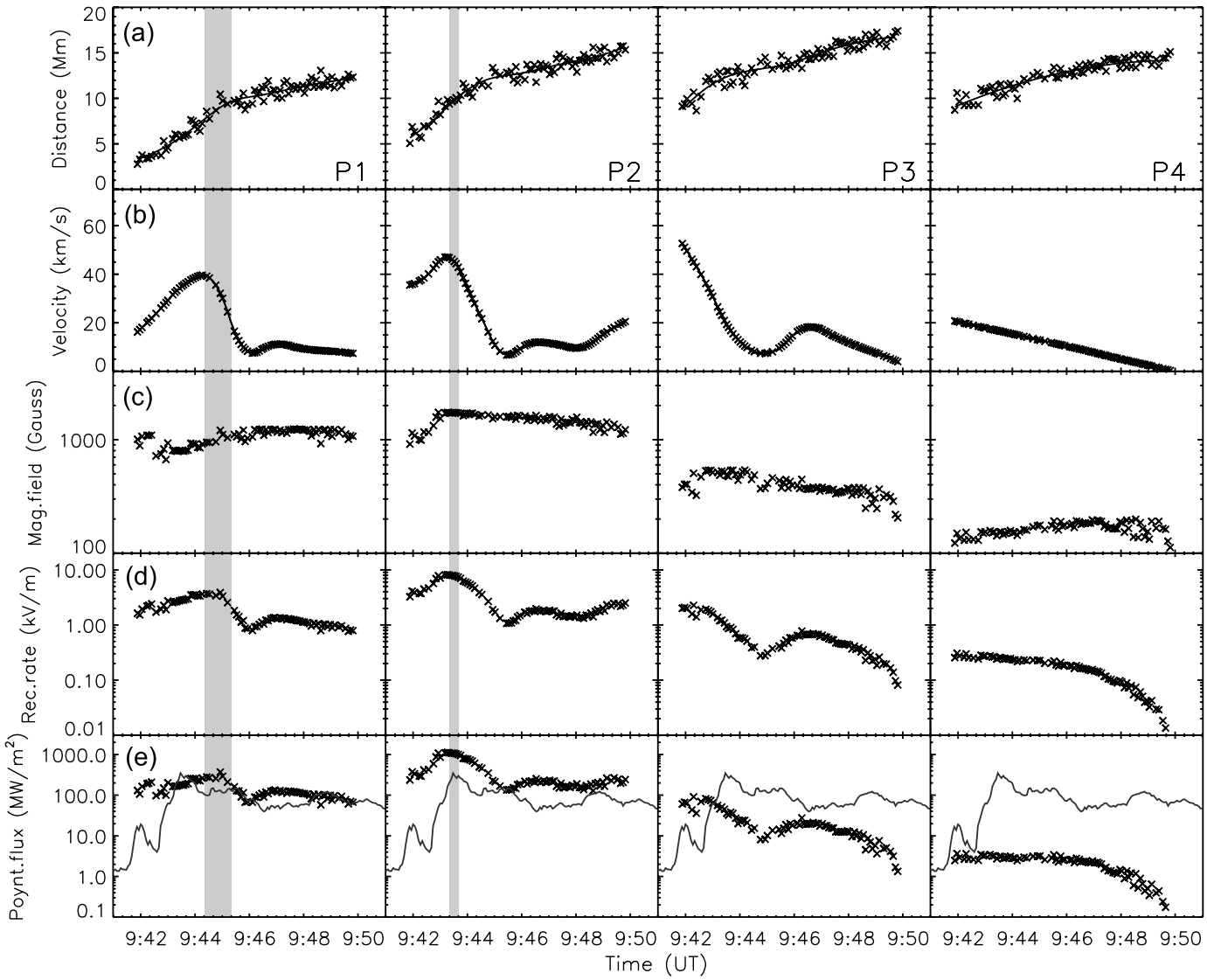

FIG. 5.—Expansion of the Hα ribbon associated with FP1 followed along four tracking paths (P1–P4). (*a*) Distance of the flare ribbon from the magnetic inversion line (the solid line shows the spline-smoothed curve). (*b*) Ribbon separation velocity $v_{\rm fl}$. (*c*) Absolute value of the local photospheric magnetic field B_p. (*d*) Local reconnection rate $E_c = v_{\rm fl} B_p$. (*e*) Poynting flux $S \propto v_{\rm fl} B_p^2$. The solid curve in (*e*) depicts the *RHESSI* 30–100 keV time profile (in arbitrary units). Gray bars indicate the periods where the tracked ribbon segment crosses the HXR centroids (compare Fig. 4).

four paths (P1–P4) along which the expansion of the ribbons was measured. As it can be seen from the figure, P1 and P2 were chosen to directly cross the HXR centroids at certain periods, whereas P3 and P4 lie outside the HXR centroids. However, P3 is still influenced by up to 30% of the maximum intensity of some of the HXR images; i.e., the P3 paths do not lie totally outside the HXR sources but are on their periphery. The P4 paths are at each instant outside the ∼15%–20% contour levels of the HXR sources (which we estimate to represent the noise level in the images) and can thus be considered to lie outside any HXR source.

In Figures 5 and 6 we show the results obtained from tracking the Hα flare ribbons associated with FP1 (situated in negative magnetic polarity fields) and with FP2 (positive polarity), respectively. For each tracking path we show (*a*) the distance of the outer edge of the Hα ribbon from the magnetic inversion line, (*b*) the velocity $v_{\rm fl}$ of the ribbon separation derived as the time derivative of the spline-smoothed distance curve in panel *a*, (*c*) the photospheric magnetic field strength B_p at the tracked ribbon front segment, (*d*) the local reconnection rate $E_c = v_{\rm fl} B_p$, and (*e*) the Poynting flux $S = (2a/\mu) v_{\rm fl} B_p^2$, which is roughly proportional to the local energy release rate dW/dt. Note that in the plotted Poynting flux curves, the proportionality factor $a = B_c/B_p$ was simply set to unity, since we are not interested in absolute values but in the relative values for different locations on the flare ribbons. In fact, a is of course smaller than 1 (by about 1 order of magnitude; e.g., Asai et al. 2004).

The plots clearly show that the local reconnection and energy release rates are significantly higher along those segments of the flare ribbons that are accompanied by HXR sources, i.e., paths P1 and P2, than at ribbon locations where no HXR sources are observed, i.e., P4. The P3 paths that lie on the periphery of the HXR footpoints show some intermediate values lying between the other two extremes. In Table 1 we list for each tracking path (P1–P4) the maximum distance of the flare ribbon expansion ($d_{\rm max} - d_{\rm min}$) and the minimum and maximum values of the ribbon separation velocity $v_{\rm fl}$, the underlying photospheric magnetic field B_p, the local reconnection rate (coronal electric field) E_c, and the Poynting flux S. As an estimate of the statistical errors of the measured ribbon

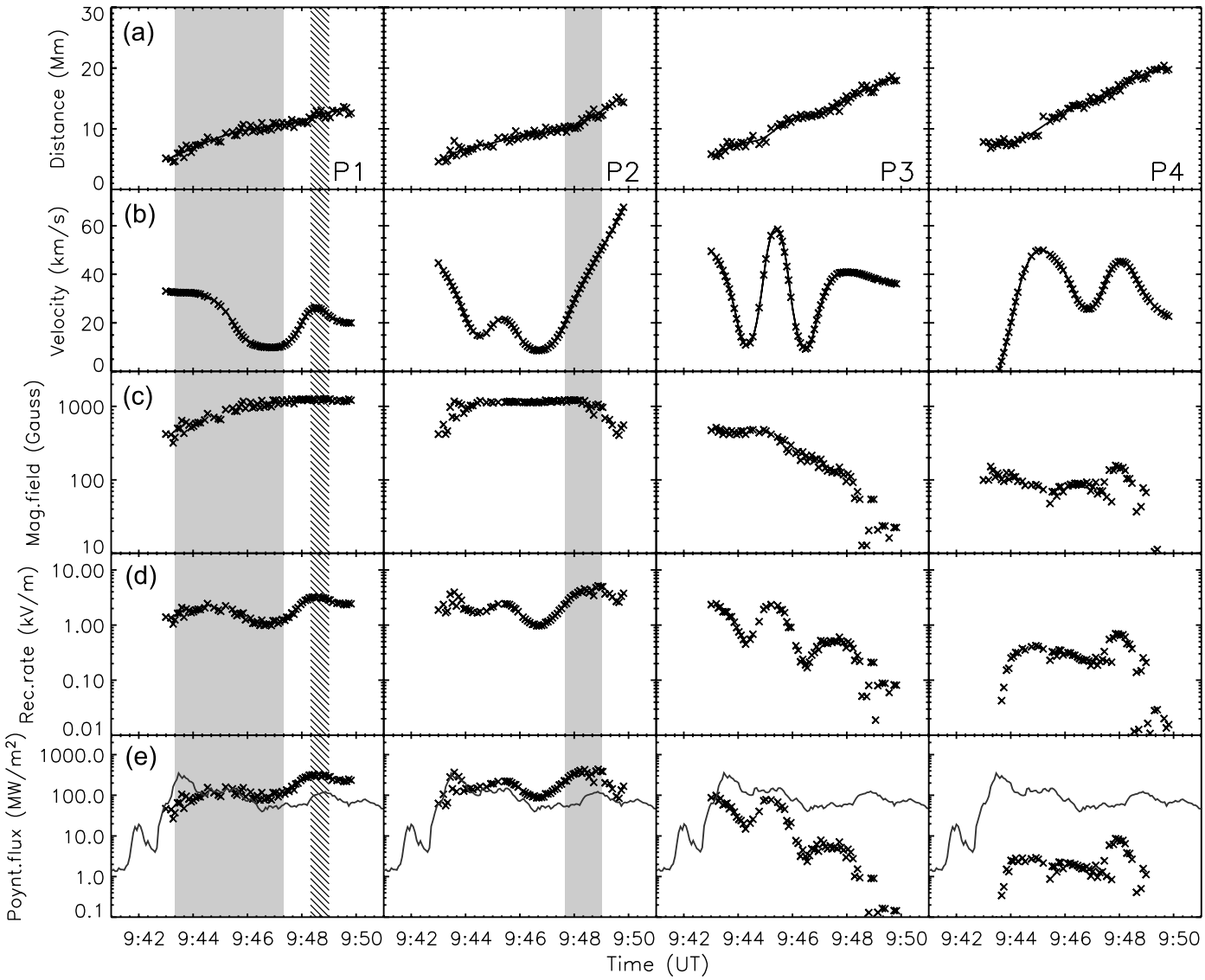

FIG. 6.—Same as Fig. 5, but for the ribbon associated with FP2. The hatched bar indicates the time when the path P1 cuts through the split FP2 source centroids.

front distances (primarily due to seeing), we derived the standard deviations of the observed data points from the spline-smoothed curves (Figs. 5 and 6), which give a relative error of about 5%. For estimating the errors on the magnetic field values at the ribbon front (primarily due to uncertainties in coregistering the Hα and magnetic field maps), we averaged over a box surrounding the identified MDI pixel, giving a relative error of about 10%–15%. Applying Gaussian error propagation, this yields relative errors on the magnetic reconnection rate E_c and the Poynting flux S of about 15%–20% and 25%–35%, respectively.

TABLE 1
DERIVED PARAMETERS FOR EACH TRACKING PATH

Associated HXR Footpoint	Path	$d_{max} - d_{min}$ (Mm)	v_{fl} (km s^{-1})		$\lvert B_p \rvert$ (G)		E_c (kV m^{-1})		S (MW m^{-2})	
			Min	Max	Min	Max	Min	Max	Min	Max
FP1	P1	10.3	7	40	670	1240	0.8	3.9	60	370
FP1	P2	10.7	7	47	910	1740	1.1	8.2	130	1130
(FP1)	P3	8.8	4	53	210	540	0.1	2.3	1	90
None	P4	6.4	<1	21	110	200	<0.01	0.3	<0.1	4
FP2	P1	9.1	10	33	320	1270	1.0	3.3	30	330
FP2	P2	10.6	9	67	410	1220	1.0	5.1	60	440
(FP2)	P3	13.2	9	58	<10	510	<0.01	2.3	<0.1	100
None	P4	14.5	<0	49	<10	220	<0.01	0.7	<0.1	10

NOTE.—P3 paths lie on the periphery of the HXR footpoints.

Figures 5 and 6 as well as Table 1 demonstrate that the very different levels of the reconnection and energy rates along P1 and P2 as compared to P4 are basically due to the much stronger magnetic fields associated with P1 and P2, which are on average about 1 order of magnitude higher than those at P4, whereas the ribbon velocity peaks lie within the same range of about 20–70 km s^{-1} for all paths, and thus only marginally contribute to the differences in E_c and S obtained for the different paths. Since the main difference between ribbon segments accompanied and those not accompanied by HXR sources lies in the associated magnetic fields B_p, the obtained differences in the Poynting flux S and the energy release rates dW/dt, which roughly scale with B_p^2, are huge: the peak values of the Poynting flux are larger by factors of ~30–300 at P1 and P2 as compared to P4 (for the overall flare phase studied, we find median values in the range 60–140). The difference in the Poynting flux peak values at P1 and P2 as compared to P3 lies in the range ~3–13.

The gray bars in the first two panels of Figures 5 and 6 indicate the periods where the ribbon front along the specific tracking paths directly crossed the HXR centroids, which were determined by the center of gravity within the 60% contour of the images' peak flux. With one exception (FP2-P1; see Figs. 6*d*–6*e*, *left panels*), the local reconnection and energy release rates reach their maximum values during these times, which provides evidence that the HXR footpoints indeed map to locations where the strongest energy release occurs (as one would expect). For FP2-P1, the reconnection and energy release rates show their highest peak at ~09:48–09:49 UT, i.e., *after* the tracking path P2 crossed the FP2 centroid, which contradicts the model expectations. However, inspecting the HXR images of FP2 in detail, applying contour levels ≳90%, the FP2 source splits up and we observe a double source. Taking into account the centroids of the split source, we find that P1 crosses one of the split FP2 centroids at ~9:48–09:49 UT (indicated by the hatched bar in Fig. 6), i.e., in accordance with the highest peaks in the reconnection and energy release rates.

We also stress that the peaks in the reconnection and energy release rates for the paths associated with HXR sources occur roughly coincident with the three highest peaks in the *RHESSI* HXR time profiles (see P1 and P2 panels in Figs. 5*e* and 6*e*). This is expected within the 2D reconnection picture if higher rates of field line reconnection in the corona produce more accelerated electrons per unit time, and thus more HXR emission (see also Krucker et al. 2005; Miklenic et al. 2006).

4. DISCUSSION AND CONCLUSIONS

The derived magnetic reconnection rates at Hα ribbon locations accompanied by HXRs lie in the range 3–8 kV m^{-1}, whereas those derived at ribbon segments without HXRs are about 1 order of magnitude smaller (0.3–0.7 kV m^{-1}). Since this difference is basically due to the different magnetic fields at these locations, which vary by almost 1 order of magnitude, the effect is even stronger for the Poynting flux and the energy release rates, which are about 2 orders of magnitude larger at HXR footpoint locations than at ribbon segments without HXRs. This finding is qualitatively consistent with the results for the X-class flare studied by Asai et al. (2002, 2004).

From a sample of 13 flares, Jing et al. (2005) found a high linear correlation between the peak value of the reconnection rate E_c and the *GOES* 1–8 Å peak flux. Comparing the peak reconnection rates reported in the literature for X-class flares (Asai et al. 2002, 2004; Qiu et al. 2004; Jing et al. 2005; the present study), we find E_c values in the range of about 0.1–8 keV m^{-1}, i.e., a scatter over almost 2 orders of magnitude. One reason for this strong scatter on top of the distinct correlation with the flare's magnitude as measured by the *GOES* classification might be that the derived reconnection rates depend strongly on the locations along the flare ribbons where they are measured. The highest reconnection rates are found at locations that are accompanied by HXRs, whereby the difference in E_c for locations with/without HXRs is about 1 order of magnitude (Asai et al. 2002, 2004; the present study).

The finding that the magnetic reconnection and energy release rates are not uniform along the flare ribbons as observed in Hα and UV, but are highest in regions where HXRs are observed, i.e., where copious amounts of accelerated electrons impinge on the chromosphere, is quite expected since it is generally well accepted that a large amount of the flare energy goes initially into accelerated electrons (e.g., Brown 1971; Lin & Hudson 1976; Wu et al. 1986; Dennis et al. 2003). Based on the derived differences for E_c and $S \propto dW/dt$ of about 1 and 2 orders of magnitude, respectively, between flare ribbons accompanied by HXRs and those without, we can now address the issue of whether these differences are large enough to explain the absence of HXR emission at certain parts of the Hα ribbon by the dynamic range of the *RHESSI* instrument. *RHESSI* has a dynamic range that may be as good as ~20:1 for events with good count statistics (Hurford et al. 2002). This means that sources with a surface brightness of ≲5% of the brightest source can no longer be observed. More complicated source morphologies (like in the present flare, where up to four individual HXR sources were present simultaneously) may result in a still lower dynamic range.

The released magnetic energy rate dW/dt provides a measure of how much energy per unit time is available to accelerate particles to suprathermal velocities, whereas the coronal electric field E_c (magnetic reconnection rate) is basically a measure of the acceleration efficiency per particle (e.g., Lee et al. 2006). Assuming that the number of electrons per unit time that gets accelerated to suprathermal velocities is roughly proportional to the magnetic energy release rate dW/dt (which ignores the fact that more intense flares tend to have harder electron spectra), and assuming further that the power in electrons (which in detail depends on electron spectral index δ for power-law distribution and on the low-energy cutoff E_0) is roughly proportional to the observed HXR emission in a certain energy band, we can compare the differences in the derived *local* values of the energy release rate determined as $dW/dt = A_r S = \text{const} \times S$ (see § 1) for ribbon locations with/without HXRs (~30:1 up to ~300:1) with the dynamic range of the *RHESSI* HXR images (≲20:1). Since the derived differences in S and dW/dt at ribbons with/without HXRs are much larger than *RHESSI*'s dynamic range, the absence of HXR emission at certain parts of the flare ribbons can be explained by the limited dynamic range of the *RHESSI* instrument.

In this case, it is still possible that the observed Hα ribbon segments that are not accompanied with HXR footpoints are due to accelerated electrons (in contrast to other energy transport mechanisms, such as thermal conduction along the loops), but their number is too low to be observed by present X-ray instruments. The accelerated electrons are preferentially focused into a small subset (those loops outlined by the HXR footpoints) of all the loops that take part in the magnetic reconnection process (those loops outlined by the Hα ribbons and EUV postflare arcade). For the 2005 January 17 flare, we find for the ratio of the maximum flare area covered by HXR footpoints to that observed in Hα a factor of about 0.15. Using the difference in the derived *local* Poynting fluxes S between locations with/without HXRs of a factor of ~100 as a rough estimate for the different flux densities of accelerated electrons at these locations, we can estimate that the total number of electrons that goes into the small subset

of loops outlined by the HXR flare footpoints is about a factor 15 larger than those accelerated into the rest of the large flare arcade involved in the magnetic reconnection process and outlined by the Hα ribbons (and the EUV postflare loop system).[4] This implies that the "nonimaged" electrons are energetically unimportant compared to those observed by their bremsstrahlung at the HXR footpoint locations.

[4] Note that in this argument we assume that the observed flare ribbons as observed in Hα map to the complete area of the reconnecting current sheet (see Lee et al. 2006), and that the HXR areas map only to reconnection regions associated with efficient particle acceleration.

M. T. and A. V. gratefully acknowledge the Austrian *Fonds zur Förderung der wissenschaftlichen Forschung* (FWF grants J2512-N02 and P15344). The authors would like to thank the anonymous referee for helpful comments on the manuscript.

REFERENCES

Asai, A., Masuda, S., Yokoyama, T., Shimojo, M., Isobe, H., Kurokawa, H., & Shibata, K. 2002, ApJ, 578, L91
Asai, A., Yokoyama, T., Shimojo, M., Masuda, S., Kurokawa, H., & Shibata, K. 2004, ApJ, 611, 557
Berger, T. E., & Lites, B. W. 2003, Sol. Phys., 213, 213
Bogachev, S. A., Somov, B. V., Kosugi, T., & Sakao, T. 2005, ApJ, 630, 561
Brown, J. C. 1971, Sol. Phys., 18, 489
Carmichael, H. 1964, in The Physics of Solar Flares, ed. W. N. Hess (NASA SP-50; Washington, DC: NASA), 451
Czaykowska, A., de Pontieu, B., Alexander, D., & Rank, G. 1999, ApJ, 521, L75
Dennis, B. R., Veronig, A., Schwartz, R. A., Sui, L., Tolbert, A. K., Zarro, D. M., & the *RHESSI* Team. 2003, Adv. Space Res., 32, 2459
Fletcher, L., & Hudson, H. 2001, Sol. Phys., 204, 69
Fletcher, L., & Hudson, H. S. 2002, Sol. Phys., 210, 307
Forbes, T. G., & Lin, J. 2000, J. Atmos. Terr. Phys., 62, 1499
Forbes, T. G., & Priest, E. R. 1984, Sol. Phys., 94, 315
Grigis, P. C., & Benz, A. O. 2005, ApJ, 625, L143
Handy, B. N., et al. 1999, Sol. Phys., 187, 229
Hirayama, T. 1974, Sol. Phys., 34, 323
Hoyng, P., et al. 1981, ApJ, 246, L155
Hurford, G. J., et al. 2002, Sol. Phys., 210, 61
Isobe, H., Yokoyama, T., Shimojo, M., Morimoto, T., Kozu, H., Eto, S., Narukage, N., & Shibata, K. 2002, ApJ, 566, 528
Jing, J., Qiu, J., Lin, J., Qu, M., Xu, Y., & Wang, H. 2005, ApJ, 620, 1085
Kašparová, J., Karlický, M., Kontar, E. P., Schwartz, R. A., & Dennis, B. R. 2005, Sol. Phys., 232, 63
Kitahara, T., & Kurokawa, H. 1990, Sol. Phys., 125, 321
Kopp, R. A., & Pneuman, G. W. 1976, Sol. Phys., 50, 85
Krucker, S., Fivian, M. D., & Lin, R. P. 2005, Adv. Space Res., 35, 1707
Krucker, S., Hurford, G. J., & Lin, R. P. 2003, ApJ, 595, L103
Lee, J., Gary, D. E., & Choe, G. S. 2006, ApJ, 647, 638
Lin, R. P., & Hudson, H. S. 1976, Sol. Phys., 50, 153
Lin, R. P., Krucker, S., Holman, G. D., Sui, L., Hurford, G. J., & Schwartz, R. A. 2003, in Proc. 28th Int. Cosmic Ray Conf. (Tsukuba), 3207
Lin, R. P., et al. 2002, Sol. Phys., 210, 3
Masuda, S., Kosugi, T., Hara, H., Tsuneta, S., & Ogawara, Y. 1994, Nature, 371, 495
Masuda, S., Kosugi, T., & Hudson, H. S. 2001, Sol. Phys., 204, 55
Miklenic, C., Veronig, A. M., Vršnak, B., & Hanslmeier, A. 2006, A&A, submitted
Otruba, W. 2005, Hvar Obs. Bull., 29, 279
Otruba, W., & Pötzi, W. 2003, Hvar Obs. Bull., 27, 189
Qiu, J., Wang, H., Cheng, C. Z., & Gary, D. E. 2004, ApJ, 604, 900
Sakao, T. 1994, Ph.D. thesis, Univ. Tokyo
Sakao, T., Kosugi, T., & Masuda, S. 1998, in Observational Plasma Astrophysics: Five Years of *Yohkoh* and Beyond, ed. T. Watanabe & T. Kosugi (Dordrecht: Kluwer), 273
Sakao, T., et al. 1992, PASJ, 44, L83
Scherrer, P. H., et al. 1995, Sol. Phys., 162, 129
Smith, D. M., et al. 2002, Sol. Phys., 210, 33
Sturrock, P. A. 1966, Nature, 211, 695
Sui, L., Holman, G. D., & Dennis, B. R. 2004, ApJ, 612, 546
Švestka, Z. 1996, Sol. Phys., 169, 403
Švestka, Z. F., Fontenla, J. M., Machado, M. E., Martin, S. F., & Neidig, D. F. 1987, Sol. Phys., 108, 237
Tsuneta, S., Hara, H., Shimizu, T., Acton, L. W., Strong, K. T., Hudson, H. S., & Ogawara, Y. 1992, PASJ, 44, L63
Veronig, A. M., & Brown, J. C. 2004, ApJ, 603, L117
Veronig, A. M., Karlický, M., Vršnak, B., Temmer, M., Magdalenić, J., Dennis, B. R., Otruba, W., & Pötzi, W. 2006a, A&A, 446, 675
Veronig, A. M., Temmer, M., Vršnak, B., & Thalmann, J. K. 2006b, ApJ, 647, 1466
Vršnak, B., Temmer, M., Veronig, A., Karlický, M., & Lin, J. 2006, Sol. Phys., 234, 273
Wu, S. T., et al. 1986, in Energetic Phenomena on the Sun, ed. M. R. Kundu & B. Woodgate (NASA CP-2439; Washington, DC: NASA), 5-5